



# Effects of Ag substitution for Fe on glass-forming ability, crystallization kinetics, and mechanical properties of Ni-free Zr–Cu–Al–Fe bulk metallic glasses

B. Li , W.C. Sun , H.N. Qi , J.W. Lv , F.L. Wang , M.Z. Ma <sup>\*</sup> , X.Y. Zhang

State Key Laboratory of Metastable Materials Science and Technology, Yanshan University, Qinhuangdao, 066004, China



## ARTICLE INFO

### Article history:

Received 20 December 2019

Received in revised form

7 February 2020

Accepted 14 February 2020

Available online 15 February 2020

### Keywords:

Zr-based bulk metallic glasses

Glass-forming ability

Crystallization kinetics

Mechanical properties

## ABSTRACT

In present study, the effects of the substitution of Ag for Fe on the glass-forming ability (GFA), crystallization kinetics, and mechanical properties of  $Zr_{60}Cu_{25}Al_{10}Fe_{5-x}Ag_x$  ( $x = 0, 1, 2, 3, 4$ , and  $5$  at%) bulk metallic glasses (BMGs) were investigated. Under the same experimental conditions, the critical diameter for glass formation increased significantly by appropriately substituting Ag for Fe. The activation energies, including  $E_g$ ,  $E_x$ , and  $E_p$ , all increased significantly, which indicated that Ag addition reduced the sensitivity of the amorphous alloys to temperature, as well as increased the energy barriers of atom rearrangements, nucleation and growth, i.e., the stability of the BMG enhanced. In addition, the plasticity of the alloys was enhanced thanks to the substitution. The plastic strain reached 3.7% when the content of Ag was 4 at%, which is nearly 10 times higher than the original composition (0.4%).

© 2020 Elsevier B.V. All rights reserved.

## 1. Introduction

Bulk metallic glasses (BMGs) have a very broad application prospect because of their unique characteristics such as high hardness, high elasticity, high wear resistance, high corrosion resistance, and superplasticity [1–4]. After their initial discovery in the 1980s, BMGs have attracted considerable attention. A large number of amorphous alloy systems such as Ti-based [1], Mg-based [1], Pd-based [5], Zr-based [6], and Fe-based [7] BMGs have been developed; therefore, there are many potential application scenarios of BMGs. Zr-based BMGs have a high potential and have attracted considerable attention because of their low cost, high glass-forming ability (GFA), low critical cooling speed, low Young's modulus, and good biocompatibility [8–13]. However, toxic elements, such as Be and Ni, are often associated with the high GFA of Zr-based BMGs, which considerably limits their application prospects, especially in the field of biomaterials [9]. Thus, the development of Zr-based BMGs with a good GFA but without Ni and Be is significant. In the previous works, many Ni- and Be-free Zr-based amorphous alloy systems have been developed and studied, especially the Zr–Cu–Fe–Al system [14,15]. Louzguine-luzgin et al. not

only studied the devitrification behavior and structural changes of Zr–Cu–Fe–Al amorphous alloys on heating, but also found that the alloys had no thermal embrittlement because of the phase separation phenomenon during heating [16,17]. Using specific methods to perform compression tests on Zr–Cu–Fe–Al amorphous alloys, Zhang et al. explored the formation and flow behavior of shear bands during the deformation of BMGs [18]. However, the GFA and plasticity of these BMGs need to be improved further.

To optimize various properties of BMGs, such as the GFA, mechanical properties, stability, and soft magnetic properties, micro-alloying is often an important solution [19–25]. Note that Ag is a very common minor element. Zhang et al. reported that adding Ag in Cu–Zr amorphous alloys could remarkably enhance its thermodynamic stability and GFA [26]. Using an experimental and molecular dynamics (MD) simulation, Kim et al. reported that adding Ag in  $(Cu_{0.5}Zr_{0.5})_{100-x}Ag_x$  led to heterogeneity at the atomic dimension level and introduced a large number of stable icosahedral short-range ordering (ISRO) structures, which resulted in the simultaneous improvement of GFA, strength, and plasticity of the alloy [27]. Rahvard et al. reported that when 4% Ag was added to the Zr–Co–Al BMGs, the kinetic stability of the alloy considerably improved [28].

In this study, using  $Zr_{60}Cu_{25}Al_{10}Fe_5$  as the basis, a new amorphous alloy system  $Zr_{60}Cu_{25}Al_{10}Fe_{5-x}Ag_x$  ( $x = 0, 1, 2, 3, 4$ , and  $5$  at%) was obtained by gradually replacing Fe with Ag. The effects of the

\* Corresponding author.

E-mail address: [mz550509@ysu.edu.cn](mailto:mz550509@ysu.edu.cn) (M.Z. Ma).

substitution were examined by studying the GFA, crystallization kinetics, and mechanical properties.

## 2. Experimental

Alloy ingots with nominal compositions  $Zr_{60}Cu_{25}Al_{10}Fe_{5-x}Ag_x$  ( $x = 0, 1, 2, 3, 4$ , and  $5$  at%) were prepared by arc melting the raw materials (purity  $\geq 99.9\%$ ). To ensure a homogeneous composition, the ingots were inverted and remelted five times. Then, a series of rods with a length of  $70$  mm and diameters of  $3, 4, 5, 6$ , and  $8$  mm were obtained by copper mode suction-casting. The microstructures of these as-cast alloy rods were analyzed using X-

ray diffraction (XRD, D/max-2500/PC) with Cu radiation and transmission electron microscopy (TEM, JOEL2010). Differential scanning calorimetry (DSC, Netzsch 404 F3) experiments at a series of heat rates ( $5, 10, 20, 30$ , and  $40$  K/min) were performed in the temperature range of  $30$ – $1000$  °C under a continuous Ar flow to examine the thermodynamic and kinetic properties of the alloys. The test samples, having a weight of  $10$ – $20$  mg, were cut from amorphous alloy rods with a diameter of  $3$  mm of each composition and ultrasonically cleaned in alcohol for  $30$  min. For analyzing the mechanical properties of BMGs, uniaxial compression tests were

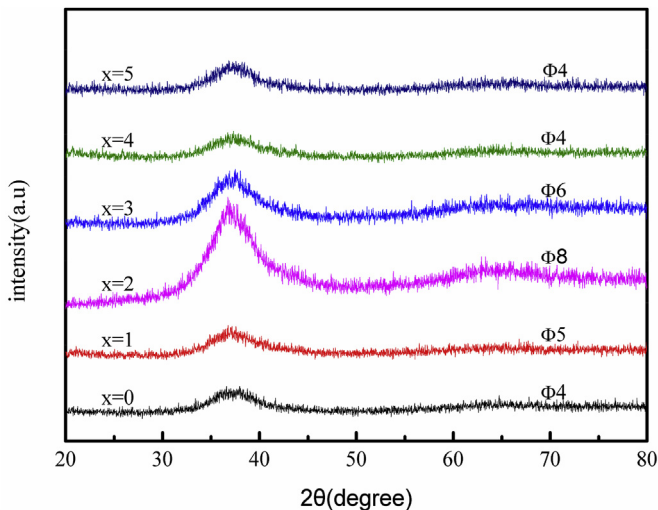


**Fig. 1.** XRD patterns of  $Zr_{60}Cu_{25}Al_{10}Fe_{5-x}Ag_x$  ( $x = 0, 1, 2, 3, 4$ , and  $5$  at%) rods with each critical diameter.

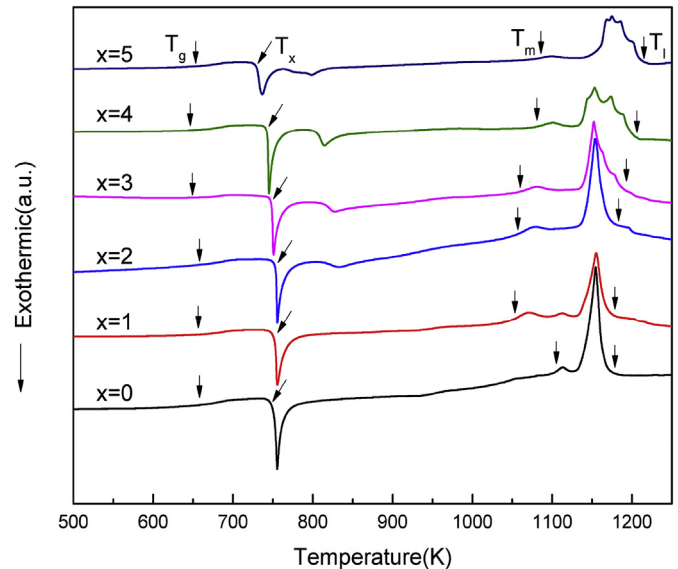


**Fig. 3.** DSC curves of  $Zr_{60}Cu_{25}Al_{10}Fe_{5-x}Ag_x$  ( $x = 0, 1, 2, 3, 4$ , and  $5$  at%) with a heating rate of  $20$  K/min.

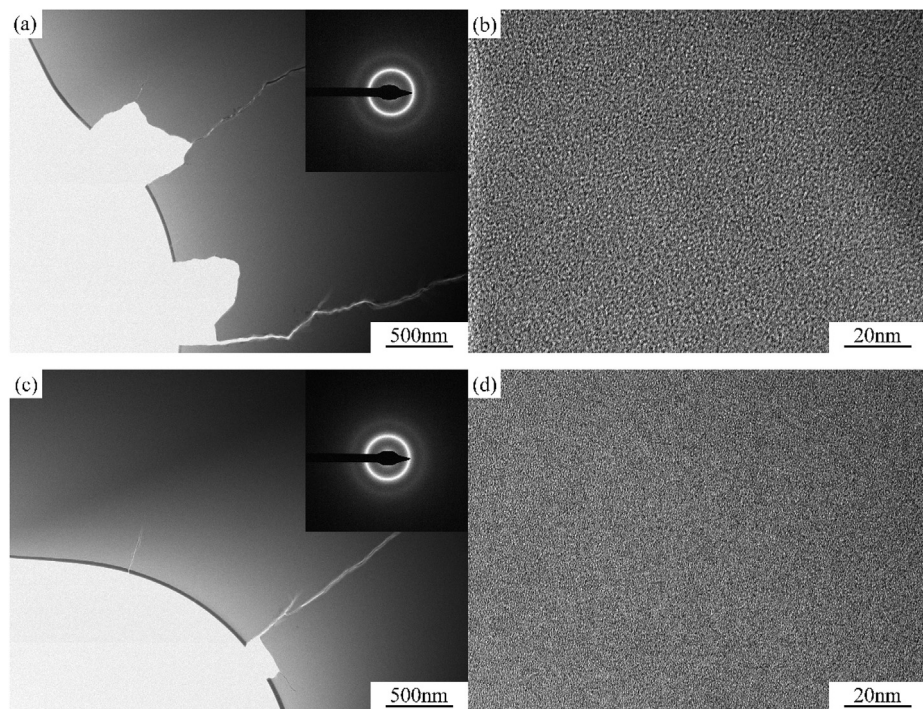


**Fig. 2.** Bright-field TEM/HRTEM images and selected area electron diffraction (SAED) patterns of the  $Zr_{60}Cu_{25}Al_{10}Fe_{5-x}Ag_x$  ( $x = 0$  and  $2$ ) alloys with the critical diameters: (a), (b)  $x = 0$ ,  $\Phi 4$  mm; (c), (d)  $x = 2$ ,  $\Phi 8$  mm.

**Table 1**

Thermal parameters of  $Zr_{60}Cu_{25}Al_{10}Fe_{5-x}Ag_x$  ( $x = 0, 1, 2, 3, 4$ , and  $5$  at%) with a heating rate of  $20$  K/min.

Alloys	$T_g/K$	$T_x/K$	$T_m/K$	$T_l/K$	$\Delta T_x/K$	$T_r$	$\gamma$
$x = 0$	668.2	750.7	1102.4	1179.9	82.5	0.606	0.406
$x = 1$	668.3	753	1078	1180.4	84.7	0.619	0.407
$x = 2$	667.3	754.6	1052.2	1182	87.3	0.634	0.408
$x = 3$	665.5	748.9	1055.4	1201.6	83.4	0.631	0.401
$x = 4$	664.7	741.5	1079.2	1207.9	76.8	0.616	0.396
$x = 5$	660	729.8	1072.9	1209	69.8	0.615	0.390

performed using a universal testing machine (Instron-5982) at a strain rate of  $5 \times 10^{-4}$  s $^{-1}$ . The samples were BMG rods with a diameter of  $3$  mm and a length of  $6$  mm. To ensure data reliability, each compression test was repeated more than  $5$  times. Then, the lateral surfaces and fracture morphologies of the samples after compressional tests were then observed using a scanning electron microscope (SEM, Hitachi S-3400).

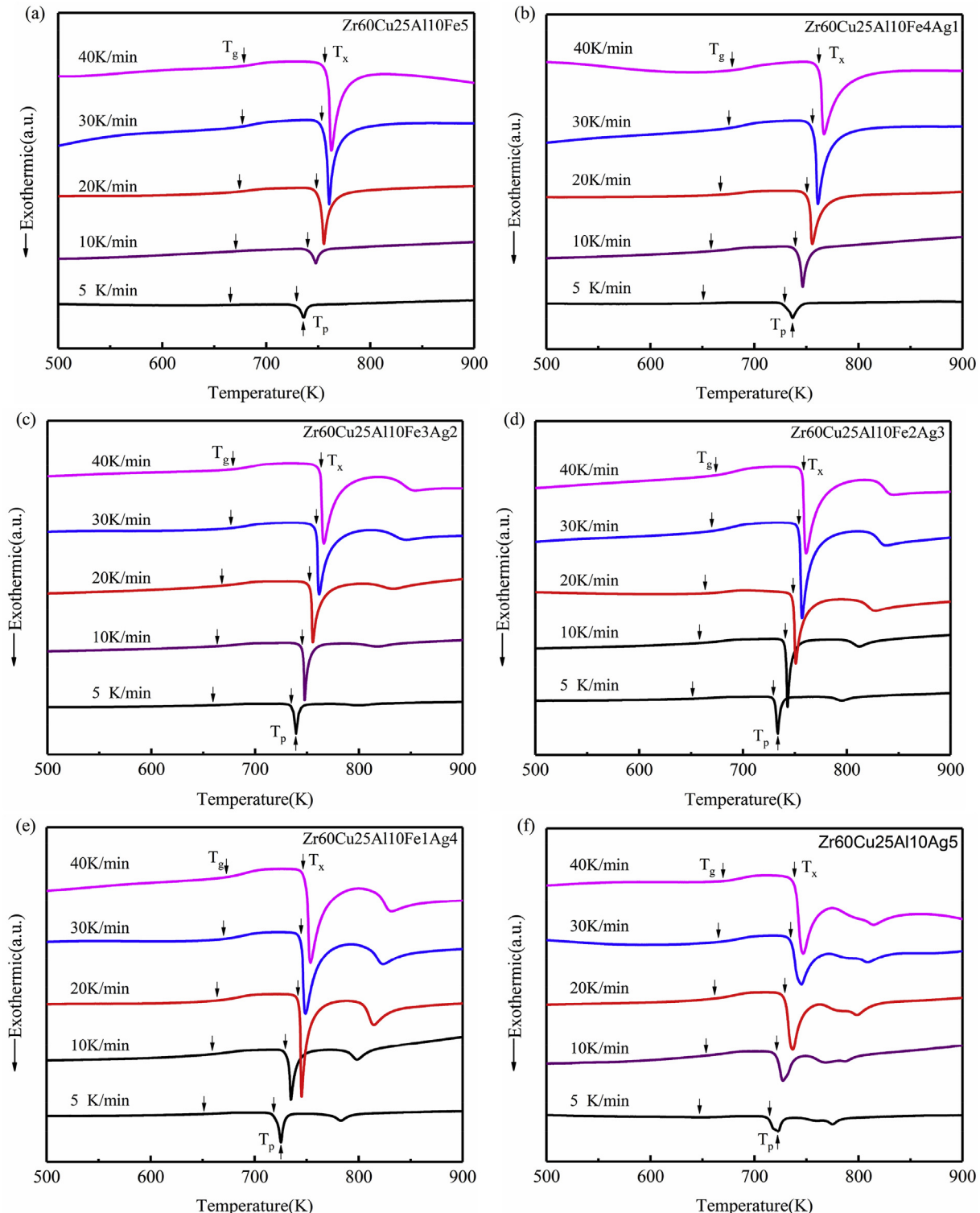


**Fig. 4.** The DSC curves of  $Zr_{60}Cu_{25}Al_{10}Fe_{5-x}Ag_x$  ( $x = 0, 1, 2, 3, 4$  and  $5$  at%) at different heating rates: (a)  $x = 0$ , (b)  $x = 1$ , (c)  $x = 2$ , (d)  $x = 3$ , (e)  $x = 4$ , and (f)  $x = 5$ .

**Table 2**

Character temperatures of  $Zr_{60}Cu_{25}Al_{10}Fe_{5-x}Ag_x$  ( $x = 0, 1, 2, 3, 4$ , and  $5$  at%) at different heating rates.

alloys	$\beta$ (K/min)	$T_g$ (K)	$T_x$ (K)	$T_p$ (K)	$\Delta T_x$ (K)
$x = 0$	5	653.4	631.5	635.6	78.1
	10	662.1	741.1	744.6	79
	20	668.2	750.7	755.7	82.5
	30	674.2	757.1	761	82.9
	40	675.7	760.1	763.5	84.4
$x = 1$	5	654.5	732.9	736.8	78.4
	10	661.8	742.6	747	80.8
	20	668.3	753	755.6	84.7
	30	671.9	758.2	761	86.3
	40	675.8	762.4	766.9	86.6
$x = 2$	5	655.8	737	739	81.2
	10	662.5	746.5	747.3	84
	20	667.3	754.6	755.9	87.3
	30	670.8	759.6	762	88.4
	40	675.4	763.5	765.3	88.1
$x = 3$	5	651.7	731.4	733.4	79.7
	10	658.4	740.9	742.9	82.5
	20	665.5	748.9	750.8	83.4
	30	669	754.7	756.9	85.7
	40	672	758.5	761.1	86.5
$x = 4$	5	650.8	722.8	726.1	72
	10	659.1	732.5	734.9	73.4
	20	664.7	741.5	745.2	76.8
	30	669	745.4	749	76.4
	40	673.3	751	753.7	77.7
$x = 5$	5	645.5	707.6	716	62.1
	10	653.9	718.3	725.2	64.4
	20	660	729.8	736.9	69.8
	30	665.3	735.6	745.2	70.3
	40	669.7	739.4	747.1	69.7

### 3. Results and discussion

#### 3.1. Glass-forming ability

Fig. 1 shows the typical XRD patterns of  $Zr_{60}Cu_{25}Al_{10}Fe_{5-x}Ag_x$  ( $x = 0, 1, 2, 3, 4$ , and  $5$  at%) BMG samples obtained from the respective largest size amorphous alloy rods under the same experimental conditions. Each pattern had only one broad diffraction peak without any visible crystalline peak, which confirmed the amorphous structure of the specimens. Moreover, this behavior shows that, with a gradual increase in Ag content, the alloys' critical size for glass forming first increased, reached a maximum of 8 mm when  $x = 2$  at%, and then decreased. This behavior indicates that appropriate substitution significantly enhanced the GFA of the amorphous alloy system. Fig. 2 shows the bright-field TEM images, selected area electron diffraction (SAED) patterns, and high-resolution transmission electron microscopy (HRTEM) images of  $Zr_{60}Cu_{25}Al_{10}Fe_5$  (4 mm) and  $Zr_{60}Cu_{25}Al_{10}Fe_3Ag_2$  (8 mm). There were no crystalline fringes or phase separation in the bright-field TEM and HRTEM images, moreover, the SAED patterns showed a broad halo, which confirmed the amorphous structure of the samples.

Fig. 3 shows the DSC curves of  $Zr_{60}Cu_{25}Al_{10}Fe_{5-x}Ag_x$  ( $x = 0, 1, 2, 3, 4$ , and  $5$  at%) amorphous alloys at a heating rate of 20 K/min. The characteristic temperatures and other important parameters, such as glass transition temperature ( $T_g$ ), onset temperature of crystallization ( $T_x$ ), melting temperature ( $T_m$ ), liquidus temperature ( $T_l$ ), supercooled liquid region ( $\Delta T_x = T_x - T_g$ ), reduced glass transition temperature ( $T_r = T_g/T_m$ ), and  $\gamma$  value ( $\gamma = T_x/(T_l + T_g)$ ) are listed in Table 1. Inoue et al. reported that  $\Delta T_x$  can reflect the GFA and the

stability of melt under the supercooled state for BMGs to some extent [29]. Note that  $T_r$  is Turnbull's criterion for the GFA of alloy liquids, which is determined using the classical nucleation theory [30]. The  $\gamma$  value is a simple indicator of GFA, which is positively correlated to the GFA of BMGs [31]. As shown in Table 1, with the gradual increase in Ag content, the values of  $\Delta T_x$ ,  $T_p$ , and  $\gamma$  increased first, and then decreased. Moreover, when  $x = 2$ , all the values were maximized: they increased from 82.8 K, 0.606, and 0.406 for the master alloy to 87.3 K, 0.634, and 0.408, respectively; these values are basically in line with the changing GFA trend.

Previous studies demonstrated that adding certain elements having a large mixed enthalpy difference with the primary elements for an amorphous alloy can lead to atomic-scale component segregation during cooling and promote the formation of stable ISRO structures, thus resulting in the GFA improvement for BMGs [27,32,33]. In this study, the mixed enthalpies of Ag–Zr, Ag–Cu, Ag–Al, and Ag–Fe pairs were  $-20$ ,  $2$ ,  $-4$ , and  $28$  kJ/mol, respectively [34]. Because of the difference in mixed enthalpy between Ag and the primary elements of the system, adding Ag may introduce a large number of strong icosahedral structures and thus significantly improve the GFA of the system. By combining experiments with molecular dynamics (MD) simulations, Kim et al. demonstrated that, because of the considerable difference in the mixed enthalpy between Ag–Zr and Ag–Cu atom pairs, the addition of a small amount of Ag into a Zr–Cu binary amorphous alloy would promote the formation of a large number of densely packed short-range orders (SROs), such as stable icosahedral SROs and distorted icosahedra SROs, and result in a remarkable enhancement in the GFA and mechanical properties [27]. Hua et al. reported that in  $Zr_{56}Al_{16}(Ni_{1-x}Ag_x)_{28}$ , because of the addition of Ag, various SROs, which significantly changed the microstructure of the system, increased both the atomic stacking density and GFA [35]. The mixed enthalpy of the Ag–Ni pair (15 kJ/mol) and that of the Ag–Fe pair were very close, and both have a considerable difference from that of Zr–Ag and Al–Ag pairs. These reports provide reliable examples for the present study. Furthermore, for icosahedron clusters with a coordination number of 12, the ideal ratio of atomic radius between solute and solvent atoms was 0.9 [36]. In this study, the atomic radius ratios ( $R$ ) are  $R(Fe/Zr) = 0.78$  and  $R(Ag/Zr) = 0.91$ ; therefore, the Ag-bearing alloys of the system possibly form ISRO structures compared to the original composition from the point of efficient atom packing view [28].

In addition, Ag prefers to form atom pairs with Zr and Al during the cooling process because of their negative mixed enthalpies, which could impede the crystallization process and stabilize the supercooled liquid [37]. Nevertheless, with a continuous increase in Ag content, the positive mixed enthalpy of the Ag–Cu atom pair would lead to the deterioration of the strong atomic bonding configuration of the amorphous alloys [38]. Hence, when the concentration of Ag exceeded 2 at%, the GFA decreased with the content increasing because the detrimental effect played a dominant role.

#### 3.2. Crystallization kinetics

Fig. 4 shows the DSC curves of  $Zr_{60}Cu_{25}Al_{10}Fe_{5-x}Ag_x$  ( $x = 0, 1, 2, 3, 4$ , and  $5$  at%) alloys at different heating rates (5, 10, 20, 30, and 40 K/min). When the Ag content was  $<2$  at%, only one exothermic peak was visible at all heating rates; however, when the content of Ag surpassed 2 at%, a small exothermic peak appeared after a complete exothermic peak. This shows that the addition of Ag significantly changed the heating crystallization process of the amorphous alloys. Note that the exact mechanism of this process is unclear and will be further examined in the future. Important parameters, such as  $T_g$ ,  $T_x$ ,  $T_p$ , and  $\Delta T_x$ , are listed in Table 2. Obviously, the values of  $T_g$ ,  $T_x$ ,  $T_p$ , and  $\Delta T_x$  increased as the heating rates increased, indicating that

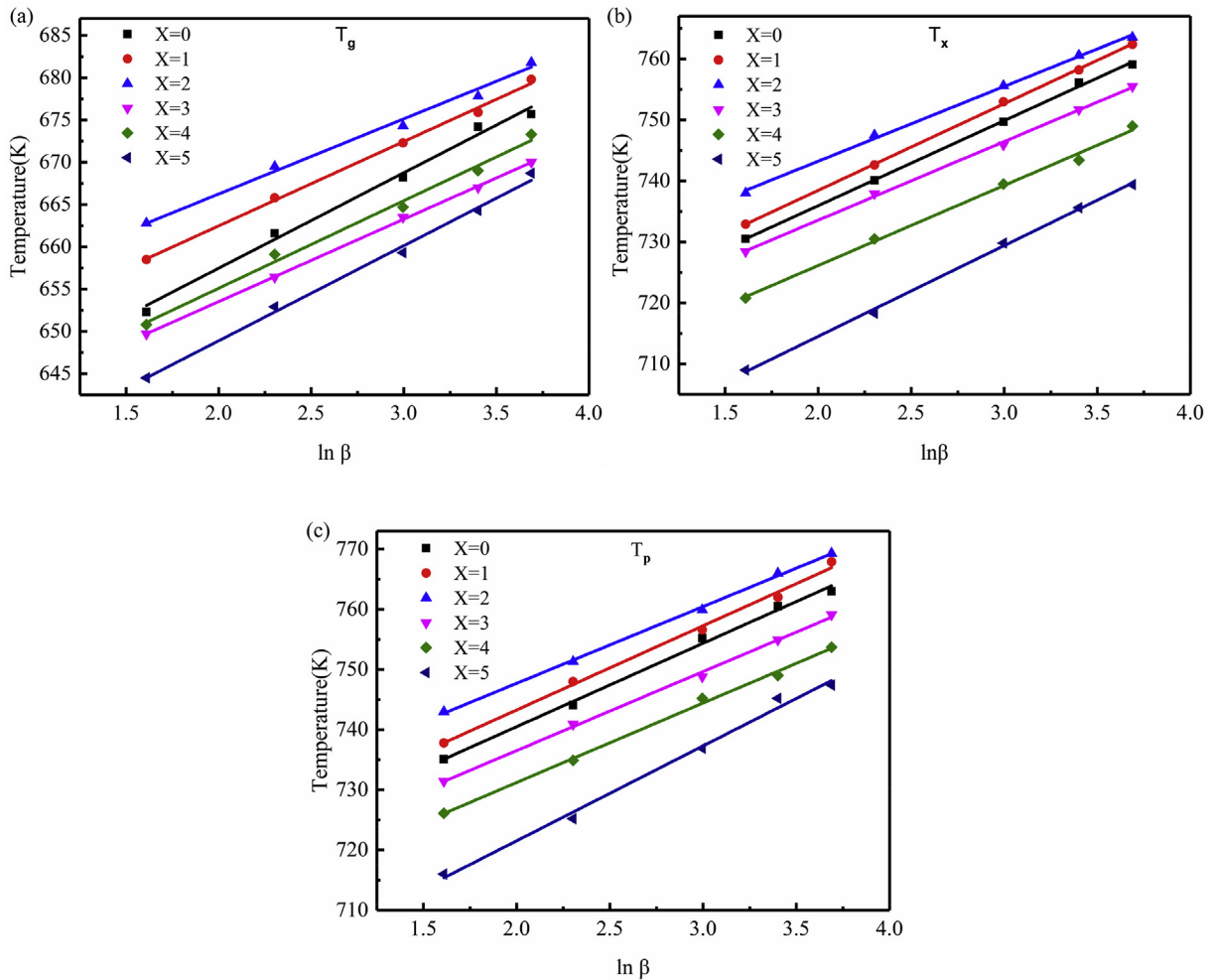


**Fig. 5.** The plots of  $\ln(\beta)$  versus  $T_g$  (a),  $T_x$  (b), and  $T_p$  (c) of  $Zr_{60}Cu_{25}Al_{10}Fe_{5-x}Ag_x$  ( $x = 0, 1, 2, 3, 4$ , and  $5$  at%). The fits have  $R^2$  values of above 0.95.

**Table 3**

The A and B values of  $Zr_{60}Cu_{25}Al_{10}Fe_{5-x}Ag_x$  ( $x = 0, 1, 2, 3, 4$ , and  $5$  at%).

alloys	parameter	$T_g$ (K)	$T_x$ (K)	$T_p$ (K)
$x = 0$	A	$635 \pm 2$	$709 \pm 1$	$713 \pm 2$
	B	$11.4 \pm 0.7$	$14.0 \pm 0.3$	$13.9 \pm 0.5$
$x = 1$	A	$638.5 \pm 1$	$710 \pm 1$	$715.3 \pm 1$
	B	$10.0 \pm 0.3$	$14.2 \pm 0.2$	$14 \pm 0.5$
$x = 2$	A	$641.5 \pm 2$	$718 \pm 1$	$722 \pm 1$
	B	$8.9 \pm 0.6$	$12.3 \pm 0.3$	$12.8 \pm 0.3$
$x = 3$	A	$636 \pm 1$	$711 \pm 1$	$710 \pm 1$
	B	$9.8 \pm 0.1$	$12.9 \pm 0.2$	$13.1 \pm 0.3$
$x = 4$	A	$634 \pm 2$	$702 \pm 1$	$705 \pm 1$
	B	$10.4 \pm 0.5$	$13.1 \pm 0.5$	$13.2 \pm 0.4$
$x = 5$	A	$627 \pm 2$	$685 \pm 1$	$690 \pm 2$
	B	$11.2 \pm 0.5$	$14.9 \pm 0.3$	$15.8 \pm 0.7$

both glass transition and crystallization processes are influenced by heating rates with obvious dynamic characteristics. However, the extent to which these characteristic temperatures varied with the variation in heating rate was different. The relation between characteristic temperature ( $T$ ) and heating rate ( $\beta$ ) can be described using Lasocka's empirical relation [39]:

$$T = A + B \ln \beta \quad (1)$$

where  $A$  and  $B$  are both constants. Fig. 5 shows the plots of characteristic temperatures ( $T_g$ ,  $T_x$ , and  $T_p$ ) versus  $\ln \beta$  for  $Zr_{60}Cu_{25}Al_{10}Fe_{5-x}Ag_x$  ( $x = 0, 1, 2, 3, 4$ , and  $5$  at%) alloys. Obviously, the  $A$  values are the Y intercept of linear fit curves, whereas the  $B$  values are positively correlated with the sensitivity of characteristic temperatures to heating rates. Based on of linear fitting results, Table 3 lists a series of values for both  $A$  and  $B$ . First, the  $B$  value of  $T_g$  is lesser than that of  $T_x$  and  $T_p$  for every alloy, indicating that the glass transition process is less sensitive to the heating rate compared to the crystallization process because the glass transition process is dependent on the relaxation process [40]. Furthermore, by comparing the  $B$  values of different components, all the three characteristic temperature temperatures of  $Zr_{60}Cu_{25}Al_{10}Fe_2Ag_2$  have the lowest sensitivity, indicating that the alloy's whole crystallization process was relatively insensitive to the heating rate. The heating rate's influence on the characteristic temperatures is closely related to activation energy  $E$  and can be expressed using Kissinger and Ozawa equation. The Kissinger equation can be expressed as follows [41]:

$$\ln\left(\frac{\beta}{T^2}\right) = -\frac{E}{RT} + C_1, \quad (2)$$

while the Ozawa equation can be expressed as follows [42]:

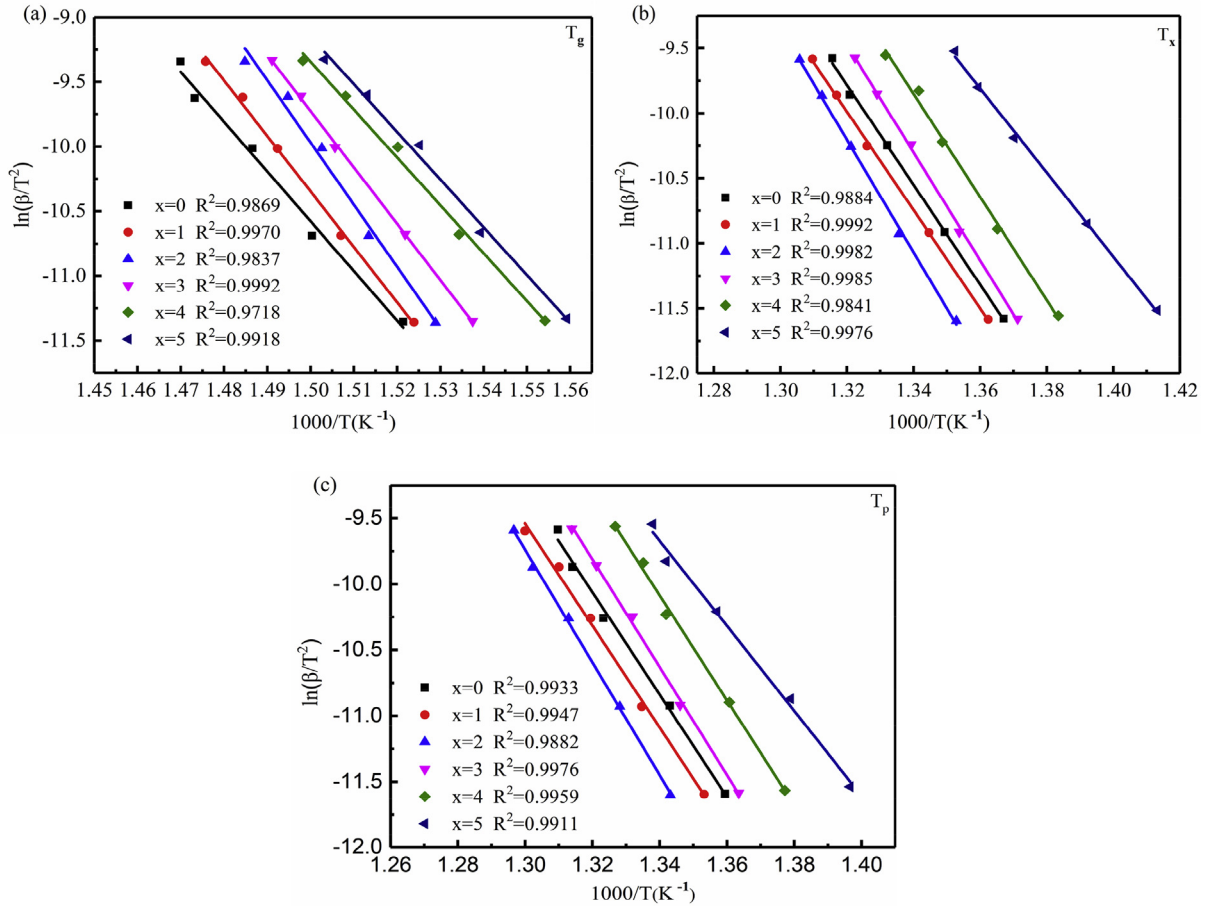


Fig. 6. Kissinger plot for (a)  $T_g$ , (b)  $T_x$ , and (c)  $T_p$ .

$$\ln(\beta) = -\frac{E}{RT} + C_1 \quad (3)$$

where  $\beta$  is the heating rate,  $T$  is the characteristic temperature, and  $C_1$  and  $C_2$  are constants. Fig. 6 and Fig. 7 show the Kissinger plot of  $\ln(\beta/T^2)$  versus  $1000/T$  and the Ozawa plot of  $\ln(\beta)$  versus  $1000/T$ , respectively. The activation energies  $E_g$ ,  $E_x$ , and  $E_p$  of the non-isothermal crystallization of  $Zr_{60}Cu_{25}Al_{10}Fe_{5-x}Ag_x$  ( $x = 0, 1, 2, 3, 4$ , and  $5$  at%) amorphous alloys can be calculated using the slopes of linear fitting curves.  $E_g$ ,  $E_x$ , and  $E_p$  represent the activation energies of the atoms rearrangement in the glass transition process, nucleation and growth in the crystallization process, respectively [28]. Table 4 shows the results obtained by different equations, and the difference between the results calculated by different methods is considerably small.

As shown by Table 4, for all alloys of  $Zr_{60}Cu_{25}Al_{10}Fe_{5-x}Ag_x$  ( $x = 0, 1, 2, 3, 4$ , and  $5$  at%), the  $E_g$  values were greater than that of  $E_x$  and  $E_p$ , suggesting that the energy barrier of the atomic rearrangement was higher than that of the nucleation and growth of crystallization. These results were consistent with those of Rahvard et al. for the Zr–Co–Al–Ag BMG system [28], Anova et al. for a series of Zr-based high-entropy BMG systems [43], and Lu et al. for the Zr–Cu–Ni–Al BMG system [44]. Moreover, the comparison between different alloys shows that, with the addition of Ag, the  $E_g$ ,  $E_x$ , and  $E_p$  of the alloys significantly increased and reached a maximum value at  $x = 2$ . The possible reasons are as follows: there are a large number of strong ISRO uniformly distributed in the 3D space in the Ag-beer alloys, which not only increased the difficulty

of atomic diffusion but also made it necessary to break the local symmetry and reorganize, followed by the improvement in the energy barriers of atomic rearrangement, nucleation, and growth processes [45].

### 3.3. Mechanical properties

Fig. 8 shows the stress–strain curves of the uniaxial compression of  $Zr_{60}Cu_{25}Al_{10}Fe_{5-x}Ag_x$  ( $x = 0, 1, 2, 3, 4$ , and  $5$  at%) amorphous alloys. Table 5 lists the various mechanical properties of each composition such as yield strength ( $\sigma_y$ ), elastic strain ( $\epsilon_e$ ), maximum strength ( $\sigma_{max}$ ), and plastic strain ( $\epsilon_p$ ). The specimens underwent a large elastic deformation ( $\epsilon_e > 2\%$ ) and then began to yield at 1720–1800 MPa, followed by a diverse degree plastic strain until fracturing occurred. The original alloy  $Zr_{60}Cu_{25}Al_{10}Fe_5$  had a large  $\sigma_y$  of 1772 MPa and a poor plastic strain of 0.4%. With the increase in Ag content, the plastic deformation of alloys was significantly enhanced while the compressive strength changed somewhat. When  $x = 2$  at%, both strength and plastic strain increased, and  $\sigma_y$  and  $\epsilon_y$  reached 1798 MPa and 1.4%, respectively. Furthermore, plastic strain reached a maximum of 3.7% when the Ag content reached 4 at%.

Fig. 9 shows the SEM images of fractured morphologies of the fractured samples. Note that all alloys showed typical vein patterns because of the unique shear deformation mode of BMGs. Both the density and distribution of veins were affected by the sample's plasticity [46]. By comparing the fractured morphologies of different composition alloys, the density of veins pattern increased

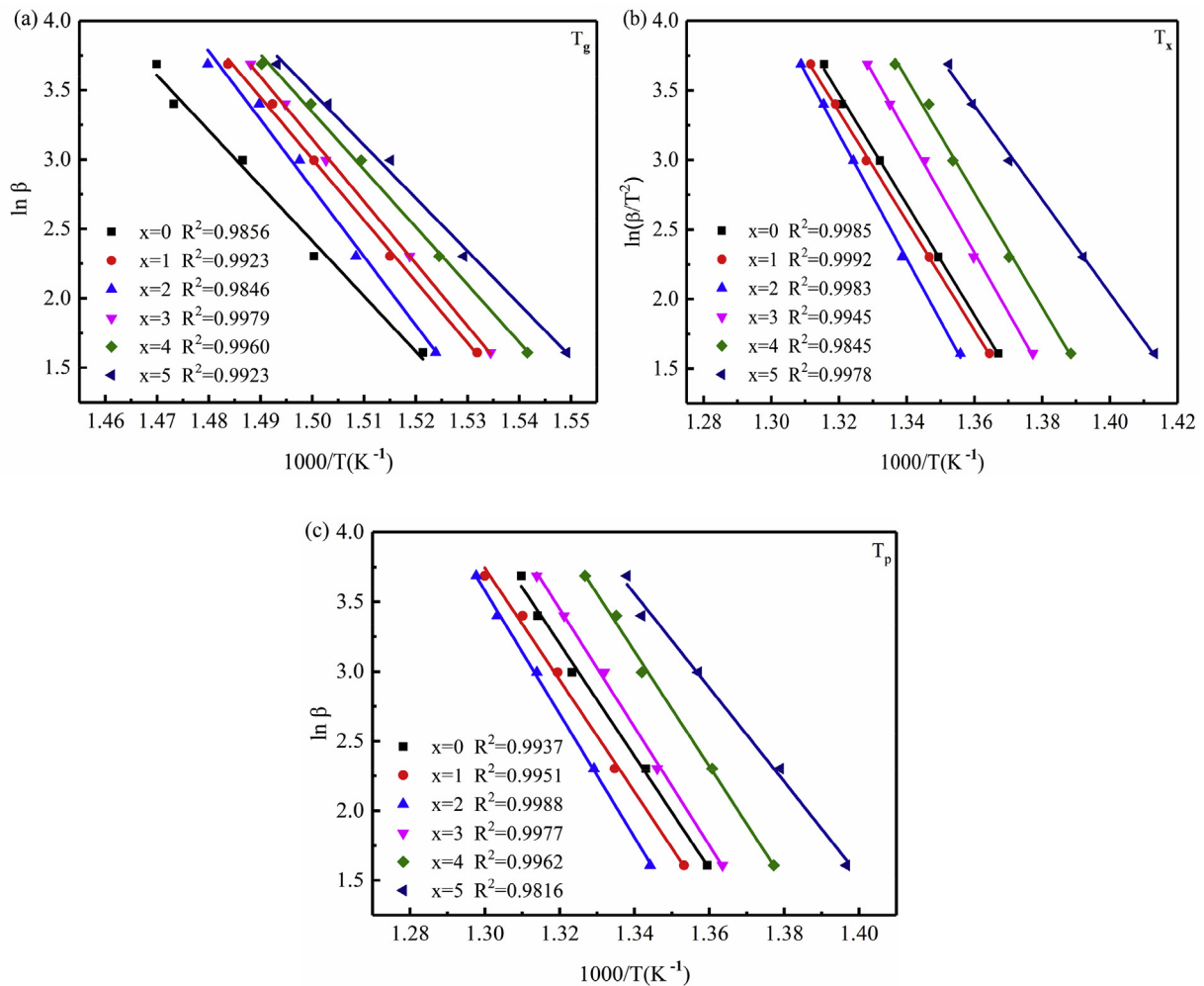


Fig. 7. Ozawa plot for (a)  $T_g$ , (b)  $T_x$ , and (c)  $T_p$ .

Table 4

The activation energies of  $Zr_{60}Cu_{25}Al_{10}Fe_{5-x}Ag_x$  ( $x = 0, 1, 2, 3, 4$ , and  $5$  at%) according to Kissinger and Ozawa equation respectively.

Alloys	$E_g(kJ/mol)$		$E_x(kJ/mol)$		$E_p(kJ/mol)$	
	Kissinger	Ozawa	Kissinger	Ozawa	Kissinger	Ozawa
$x = 0$	$325 \pm 18$	$336 \pm 18$	$319 \pm 6$	$331 \pm 6$	$323 \pm 13$	$334 \pm 13$
$x = 1$	$356 \pm 10$	$368 \pm 10$	$314 \pm 5$	$327 \pm 5$	$322 \pm 12$	$334 \pm 12$
$x = 2$	$399 \pm 26$	$410 \pm 26$	$359 \pm 8$	$372 \pm 8$	$356 \pm 6$	$368 \pm 6$
$x = 3$	$362 \pm 5$	$373 \pm 5$	$345 \pm 7$	$357 \pm 7$	$341 \pm 8$	$353 \pm 8$
$x = 4$	$334 \pm 11$	$345 \pm 11$	$319 \pm 13$	$322 \pm 13$	$331 \pm 11$	$343 \pm 11$
$x = 5$	$307 \pm 14$	$318 \pm 14$	$269 \pm 6$	$271 \pm 6$	$268 \pm 13$	$281 \pm 13$

significantly with Ag substitution for Fe, and  $Zr_{60}Cu_{25}Al_{10}Fe_1Ag_4$  showed the highest density and the most regularly distributed veins pattern, which is consistent with its good plasticity. Fig. 10 shows the SEM images of the lateral surfaces of fractured samples. In the image of  $Zr_{60}Cu_{25}Al_{10}Fe_1Ag_4$  alloy, a considerable number of interactional and multiple shear bands (SBs) emerged, which restricted the expansion along a single shear direction, thus causing the alloy to show relevant room temperature plasticity [9]. However, in  $Zr_{60}Cu_{25}Al_{10}Fe_5$ , the number of SBs was less and there is no interaction between them, which led to the rapid expansion of SBs once they are formed until they break and resulted in very low plasticity.

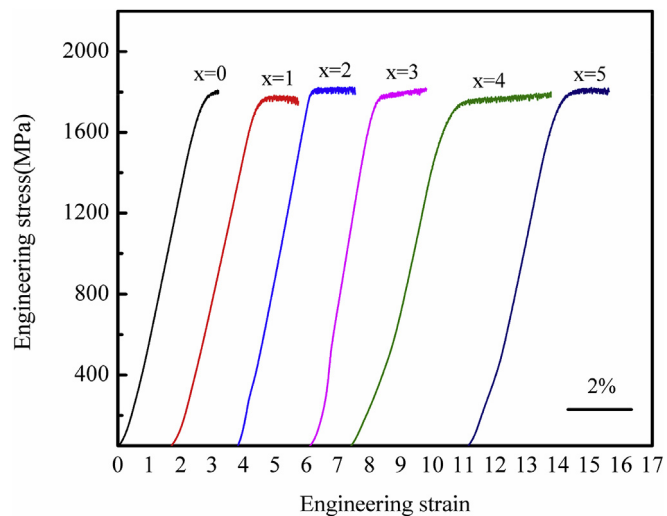


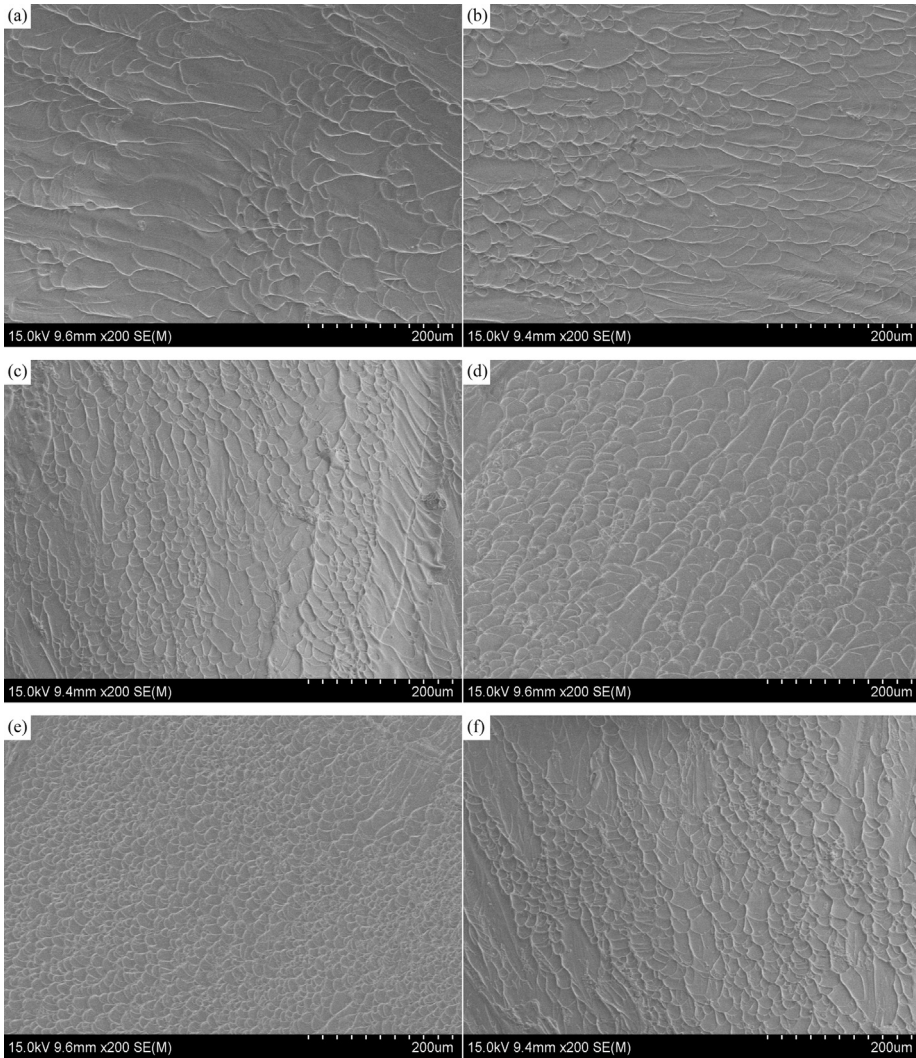
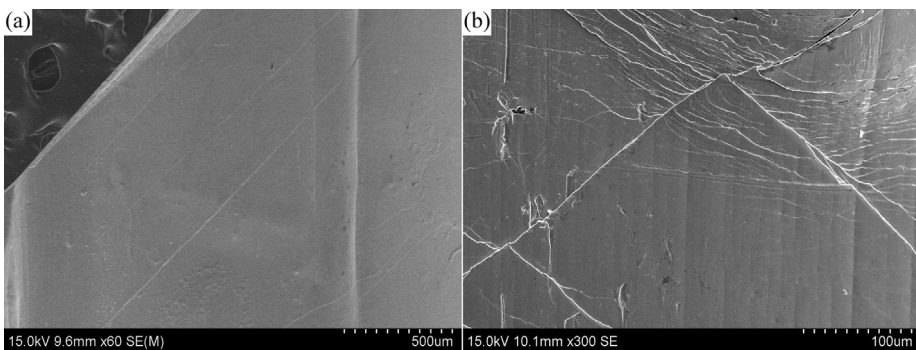
Fig. 8. The compressive engineering stress-strain curves of the  $Zr_{60}Cu_{25}Al_{10}Fe_{5-x}Ag_x$  ( $x = 0, 1, 2, 3, 4$ , and  $5$  at%).

A large mixed enthalpy difference between the minor element and the primary elements for micro-alloying would lead to atomic-scale composition segregation and resulted in an uneven

**Table 5**The mechanical properties of  $Zr_{60}Cu_{25}Al_{10}Fe_{5-x}Ag_x$  ( $x = 0, 1, 2, 3, 4$ , and  $5$  at%).

alloys	$\sigma_y$ (MPa)	$\sigma_{max}$ (MPa)	$\epsilon_e$ (%)	$\epsilon_p$ (%)
$x = 0$	$1772 \pm 27$	$1810 \pm 30$	$2.8 \pm 0.1$	$0.4 \pm 0.1$
$x = 1$	$1739 \pm 12$	$1778 \pm 10$	$2.7 \pm 0.3$	$1.3 \pm 0.4$
$x = 2$	$1798 \pm 24$	$1823 \pm 16$	$2.3 \pm 0.2$	$1.4 \pm 0.5$
$x = 3$	$1762 \pm 31$	$1820 \pm 25$	$2.1 \pm 0.1$	$1.5 \pm 0.2$
$x = 4$	$1721 \pm 29$	$1801 \pm 24$	$2.6 \pm 0.5$	$3.7 \pm 0.1$
$x = 5$	$1747 \pm 17$	$1821 \pm 15$	$2.9 \pm 0.6$	$1.5 \pm 0.2$

microstructure, which not only promoted the formation of strong ISRO structures but also encourage that of relatively weak and unstable polyhedra distributed in the 3D space of the material structure [27]. Such weak structures can be the sites of shear transformation zone (STZ) to generate, and release the local strain and resist external plastic strain; therefore, the plasticity of the BMG improved [13,27]. In this study, the difference in mixing enthalpy between Ag and the primary elements was considerably

**Fig. 9.** The fracture morphologies of  $Zr_{60}Cu_{25}Al_{10}Fe_{5-x}Ag_x$  ( $x = 1, 2, 3, 4$  and  $5$  at%): (a)  $x = 0$ , (b)  $x = 1$ , (c)  $x = 2$ , (d)  $x = 3$ , (e)  $x = 4$ , and (f)  $x = 5$ .**Fig. 10.** The SEM images of the surfaces of (a)  $Zr_{60}Cu_{25}Al_{10}Fe_5$  and (b)  $Zr_{60}Cu_{25}Al_{10}Fe_1Ag_4$ .

high. Furthermore, studies claimed that adding appropriate elements have positive mixed enthalpies with certain primary elements would obviously enhance the plasticity of BMGs because it would change the bonding structures of atoms and result in local composition inhomogeneity and change or fluctuate the distribution of local free volume in the three-dimensional space of the amorphous structure [9]. In this study, the mixed enthalpies of Cu–Ag (2 kJ/mol) and Fe–Ag (28 kJ/mol) atom pairs are positive. Moreover, the Poisson's ratio of Ag (0.38) was significantly higher than that of Fe (0.26); therefore, the Ag substitution of Fe would increase the Poisson's ratio of the alloys, which is generally positively correlated with plasticity for BMGs [47]. Thus, the plasticity of Zr<sub>60</sub>Cu<sub>25</sub>Al<sub>10</sub>Fe<sub>5</sub> amorphous alloys at room temperature was remarkably enhanced with the addition of Ag.

#### 4. Conclusions

In this study, a series of experiments and analysis were conducted to systematically study the effects of Ag substitution for Fe of Zr<sub>60</sub>Cu<sub>25</sub>Al<sub>10</sub>Fe<sub>5-x</sub>Ag<sub>x</sub> ( $x = 0, 1, 2, 3, 4$ , and  $5$  at%) BMGs. The results are as follows:

- (1) Appropriate Ag substitution for Fe can enhance the GFA of the BMGs. Under the same experimental conditions, the critical diameter for the glass formation of this system increased first and then decreased with the increase in Ag content, and then reached the maximum value of 8 mm when the content reached 2 at%. Furthermore, the values of  $\Delta T_x$ ,  $T_r$ , and  $\gamma$ , which are the common indicators of GFA and thermostability of BMGs, of Zr<sub>60</sub>Cu<sub>25</sub>Al<sub>10</sub>Fe<sub>3</sub>Ag<sub>2</sub> reached a maximum of 87.3 K, 0.634, and 0.408, respectively.
- (2) With the increase in Ag content, the activation energies  $E_g$ ,  $E_x$ , and  $E_p$  of the alloys showed an increasing trend and then decreased; moreover, they all reached a maximum when the Ag content was 2 at%, indicating that Zr<sub>60</sub>Cu<sub>25</sub>Al<sub>10</sub>Fe<sub>3</sub>Ag<sub>2</sub> had a large energy barrier in the atomic rearrangement, nucleation and growth during crystallization. Therefore, the stability of the BMG system can be significantly enhanced by the partial replacement of Fe with Ag.
- (3) The plasticity of the alloys was considerably enhanced because of the substitution of Ag for Fe. The plastic strain reached 3.7% when the content of Ag was 4 at%, which is nearly ten times higher than that of the original composition (0.4%).

#### Data availability statement

The raw/processed data required to reproduce these findings cannot be shared at this time as the data also forms part of an ongoing study.

#### Declaration of competing interest

The authors declare that they have no known competing financial interests or personal relationships that could have appeared to influence the work reported in this paper.

The authors declare the following financial interests/personal relationships which may be considered as potential competing interests: We declare that we have no known competing financial interests or personal relationships that could have appeared to influence the work reported in this paper.

We declare that we have **no** financial interests and personal relationships which may be considered as potential competing interests.

#### CRedit authorship contribution statement

**B. Li:** Conceptualization, Data curation, Methodology, Software, Investigation, Writing - original draft. **W.C. Sun:** Validation, Formal analysis, Visualization, Software. **H.N. Qi:** Validation, Formal analysis, Visualization. **J.W. Lv:** Investigation, Resources, Supervision, Data curation. **F.L. Wang:** Validation, Formal analysis, Data curation. **M.Z. Ma:** Writing - review & editing. **X.Y. Zhang:** Writing - review & editing.

#### Acknowledgements

This study was supported by the National Science Foundation of China (NSFC, Grant no.51671166/51827801), the National Key Research and Development Program of China (Grant no. 2018YFA0703603).

#### Appendix A. Supplementary data

Supplementary data to this article can be found online at <https://doi.org/10.1016/j.jallcom.2020.154385>.

#### References

- [1] A. Inoue, Stabilization of metallic supercooled liquid and bulk amorphous alloys, *Acta Mater.* 48 (2000) 279–306.
- [2] W.L. Johnson, Bulk amorphous metal—an emerging engineering material, *JOM* 54 (2002) 40–43.
- [3] W.H. Wang, C. Dong, C.H. Shek, Bulk metallic glasses, *MAT SCI ENG R* 44 (2004) 45–89.
- [4] C.J. Byrne, M. Eldrup, Bulk metallic glasses, *Science* 321 (2008) 502–503.
- [5] G.A. Kui Wh, D. Turnbull, Formation of bulk metallic glass by fluxing, *Appl. Phys. Lett.* 45 (1984).
- [6] A. Peker, W.L. Johnson, A highly processable metallic glass: Zr41.2Ti13.8-Cu12.5Ni10.0Be22.5, *Appl. Phys. Lett.* 63 (1993) 2342–2344.
- [7] H.X. Li, Z.C. Lu, S.L. Wang, Y. Wu, Z.P. Lu, Fe-based bulk metallic glasses: glass formation, fabrication, properties and applications, *Prog. Mater. Sci.* 103 (2019) 235–318.
- [8] N. Hua, S. Pang, Y. Li, J. Wang, R. Li, K. Georgarakis, A.R. Yavari, G. Vaughan, T. Zhang, Ni- and Cu-free Zr-Al-Co-Ag bulk metallic glasses with superior glass-forming ability, *J. Mater. Res.* 26 (2011) 539–546.
- [9] Z.S. Jin, Y.J. Yang, Z.P. Zhang, X.Z. Ma, J.W. Lv, F.L. Wang, M.Z. Ma, X.Y. Zhang, R.P. Liu, Effect of Hf substitution Cu on glass-forming ability, mechanical properties and corrosion resistance of Ni-free Zr-Ti-Cu-Al bulk metallic glasses, *J. Alloys Compd.* 806 (2019) 668–675.
- [10] Y.J. Yang, B.Y. Cheng, J.W. Lv, B. Li, M.Z. Ma, G. Li, R.P. Liu, Effect of Ag substitution for Ti on glass-forming ability, thermal stability and mechanical properties of Zr-based bulk metallic glasses, *Mater. Sci. Eng., A* 746 (2019) 229–238.
- [11] D.C. Jang, J.R. Greer, Transition from a strong-yet-brittle to a stronger-and-ductile state by size reduction of metallic glasses, *Nat. Mater.* 9 (2010) 215–219.
- [12] G.Y. Liu, F. Wang, Y.Y. Cao, Y. Sun, Potential prospective application of Zr-based bulk metallic glasses in dental implant, *Mater. Trans.* 56 (2015) 1925–1929.
- [13] S.S. Jiang, K.F. Gan, Y.J. Huang, P. Xue, Z.L. Ning, J.F. Sun, A.H.W. Ngan, Stochastic deformation and shear transformation zones of the glassy matrix in CuZr-based metallic-glass composites, *Int. J. Plast.* 125 (2020) 52–62.
- [14] C.L. Qiu, Q. Chen, L. Liu, K.C. Chan, J.X. Zhou, P.P. Chen, S.M. Zhang, A novel Ni-free Zr-based bulk metallic glass with enhanced plasticity and good biocompatibility, *Scripta Mater.* 55 (2006) 605–608.
- [15] K. Jin, J.F. Löffler, Bulk metallic glass formation in Zr–Cu–Fe–Al alloys, *Appl. Phys. Lett.* 86 (2005) 241909.
- [16] D.V. Louzguine-Luzgin, G. Xie, Q. Zhang, A. Inoue, Effect of Fe on the glass-forming ability, structure and devitrification behavior of Zr–Cu–Al bulk glass-forming alloys, *Phil. Mag.* 90 (2014) 1955–1968.
- [17] D.V. Louzguine-Luzgin, J. Jiang, A.I. Bazlov, V.S. Zolotorevsky, H. Mao, Y.P. Ivanov, A.L. Greer, Phase separation process preventing thermal embrittlement of a Zr–Cu–Fe–Al bulk metallic glass, *Scripta Mater.* 167 (2019) 31–36.
- [18] Q.S. Zhang, W. Zhang, G.Q. Xie, D.V. Louzguine-Luzgin, A. Inoue, Stable flowing of localized shear bands in soft bulk metallic glasses, *Acta Mater.* 58 (2010) 904–909.
- [19] H.W. Wei, Roles of minor additions in formation and properties of bulk metallic glasses, *Prog. Mater. Sci.* 52 (2007) 540–596.
- [20] N. Neuber, O. Gross, M. Eisenbart, A. Heiss, U.E. Klotz, J.P. Best, M.N. Polyakov, J. Michler, R. Busch, I. Gallino, The role of Ga addition on the thermodynamics, kinetics, and tarnishing properties of the Au–Ag–Pd–Cu–Si bulk metallic glass

- forming system, *Acta Mater.* 165 (2019) 315–326.
- [21] L. Deng, B.W. Zhou, H.S. Yang, X. Jiang, B.Y. Jiang, X.G. Zhang, Roles of minor rare-earth elements addition in formation and properties of Cu-Zr-Al bulk metallic glasses, *J. Alloys Compd.* 632 (2015) 429–434.
- [22] P. Gargarella, S. Pauly, M.S. Khoshkhooy, C.S. Kiminami, U. Kuhn, J. Eckert, Improving the glass-forming ability and plasticity of a TiCu-based bulk metallic glass composite by minor additions of Si, *J. Alloys Compd.* 663 (2016) 531–539.
- [23] N.B. Hua, W.Z. Chen, Enhancement of glass-forming ability and mechanical property of Zr-based Zr-Al-Ni bulk metallic glasses with addition of Pd, *J. Alloys Compd.* 693 (2017) 816–824.
- [24] S.D. Lu, S.C. Sun, K.H. Li, H.Y. Li, X.X. Huang, G.F. Tu, The effect of Y addition on the crystallization behaviors of Zr-Cu-Ni-Al bulk metallic glasses, *J. Alloys Compd.* 799 (2019) 501–512.
- [25] Y.J. Yang, B.Y. Cheng, Z.S. Jin, H.X. Gao, M.Z. Ma, X.Y. Zhang, Crystallization kinetics and mechanical properties of Zr<sub>56</sub>Cu<sub>24</sub>Al<sub>9</sub>Ni<sub>7</sub>-xTi<sub>4</sub>Ag<sub>x</sub> (x = 0, 1, 3, 5, and 7) metallic glasses, *J. Alloys Compd.* 816 (2020) 152589.
- [26] Z. Wei, F. Jia, Q. Zhang, A. Inoue, Effects of additional Ag on the thermal stability and glass-forming ability of Cu-Zr binary glassy alloys, *Mater. Sci. Eng., A* 459 (2007) 330–336.
- [27] H.-K. Kim, J.-P. Ahn, B.-J. Lee, K.-W. Park, J.-C. Lee, Role of atomic-scale chemical heterogeneities in improving the plasticity of Cu-Zr-Ag bulk amorphous alloys, *Acta Mater.* 157 (2018) 209–217.
- [28] M. Mohammadi Rahvard, M. Tamizifar, S.M.A. Bourtoubi, The effect of Ag addition on the non-isothermal crystallization kinetics and fragility of Zr 56 Co 28 Al 16 bulk metallic glass, *J. Non-Cryst. Solids* 481 (2018) 74–78.
- [29] A. Inoue, T. Zhang, T. Masumoto, Glass-forming ability of alloys, *J. Non-Cryst. Solids* 156–158 (1993) 473–480.
- [30] D. Turnbull, Erratum: kinetics of solidification of supercooled liquid mercury droplets, *J. Chem. Phys.* 20 (1952), 1824–1824.
- [31] D.V. Louzguine-Luzgin, G. Xie, Q. Zhang, A. Inoue, Effect of Fe on the glass-forming ability, structure and devitrification behavior of Zr–Cu–Al bulk glass-forming alloy, *Phil. Mag.* 90 (2010) 1955.
- [32] Y.S. Yun, H.S. Nam, P.-R. Cha, W.T. Kim, D.H. Kim, Effects of atomic size difference and heat of mixing parameters on the local structure of a model metallic glass system, *Met. Mater. Int.* 20 (2014) 105–111.
- [33] A. Inoue, High strength bulk amorphous alloys with low critical cooling rates (overview), *Mater. Trans., JIM* 36 (1995) 866–875.
- [34] A. Takeuchi, A. Inoue, Classification of bulk metallic glasses by atomic size difference, heat of mixing and period of constituent elements and its application to characterization of the main alloying element, *Mater. Trans.* 46 (2005) 2817–2829.
- [35] N. Hua, T. Zhang, Glass-forming ability, crystallization kinetics, mechanical property, and corrosion behavior of Zr–Al–Ni–Ag glassy alloys, *J. Alloys Compd.* 602 (2014) 339–345.
- [36] Y.Q. Cheng, E. Ma, Atomic-level structure and structure-property relationship in metallic glasses, *Prog. Mater. Sci.* 56 (2011) 379–473.
- [37] Y. Zhang, J. Yao, X. Zhao, L. Ma, Ti substituted Ni-free Zr<sub>65-x</sub>Ti<sub>x</sub>Cu<sub>17.5</sub>Fe<sub>10</sub>Al<sub>7.5</sub> bulk metallic glasses with significantly enhanced glass-forming ability and mechanical properties, *J. Alloys Compd.* 773 (2019) 713–718.
- [38] J.S.C. Jang, K.C. Wu, S.R. Jian, P.J. Hsieh, J.C. Huang, C.T. Liu, A Ni-free Zr-based bulk metallic glass with remarkable plasticity, *J. Alloys Compd.* 509 (2011) S109–S114.
- [39] M. Lasocka, The effect of scanning rate on glass transition temperature of splat-cooled Te<sub>85</sub>Ge<sub>15</sub>, *Mater. Sci. Eng.* 23 (1976) 173–177.
- [40] Y.Z. Yue, Characteristic temperatures of enthalpy relaxation in glass, *J. Non-Cryst. Solids* 354 (2008) 1112–1118.
- [41] H.E. Kissinger, Reaction Kinetics in Differential Thermal Analysis Anal. Chem. 172 (1957) 1702–1706.
- [42] T. Ozawa, Kinetic analysis of derivative curves in thermal analysis, *J. Therm. Anal.* 2 (1970) 301–324.
- [43] G. Bizhanova, F. Li, Y. Ma, P. Gong, X. Wang, Development and crystallization kinetics of novel near-equiatomic high-entropy bulk metallic glasses, *J. Alloys Compd.* 779 (2019) 474–486.
- [44] S. Lu, S. Sun, K. Li, Haiyang Li, X. Huang, G. Tu, The effect of Y addition on the crystallization behaviors of ZrCu-Ni-Al bulk metallic glasses, *J. Alloys Compd.* 799 (2019) 501–512.
- [45] W.K. Luo, H.W. Sheng, F.M. Alamgir, J.M. Bai, J.H. He, E. Ma, Icosahedral short-range order in amorphous alloys, *Phys. Rev. Lett.* 92 (2004) 4.
- [46] M. Zhou, K. Hagos, H. Huang, M. Yang, L. Ma, Improved mechanical properties and pitting corrosion resistance of Zr<sub>65</sub>Cu<sub>17.5</sub>Fe<sub>10</sub>Al<sub>7.5</sub> bulk metallic glass by isothermal annealing, *J. Non-Cryst. Solids* 452 (2016) 50–56.
- [47] Q. Dong, Y.J. Pan, J. Tan, X.M. Qin, C.J. Li, P. Gao, Z.X. Feng, M. Calin, J. Eckert, A comparative study of glass-forming ability, crystallization kinetics and mechanical properties of Zr<sub>55</sub>Co<sub>25</sub>Al<sub>20</sub> and Zr<sub>52</sub>Co<sub>25</sub>Al<sub>23</sub> bulk metallic glasses, *J. Alloys Compd.* 785 (2019) 422–428.